RSC Advances

PAPER

View Article Online
View Journal | View Issue

Cite this: *RSC Adv.*, 2022, **12**, 33108

Curcumin loaded Ag–TiO_2-halloysite nanotubes platform for combined chemo-photodynamic therapy treatment of cancer cells†

Emmanuel Nyankson, *[a] Dominic Awuzah,[a] Elvis K. Tiburu,[b] Johnson K. Efavi,[a] Benjamin Agyei-Tuffour[a] and Lily Paemka[c]

Received 13th September 2022
Accepted 15th November 2022

DOI: 10.1039/d2ra05777h

rsc.li/rsc-advances

The use of naturally occurring anticancer materials in combination with doped metal oxide has emerged as one of the most promising ways for improving anticancer treatment efficacy. In this study, the anticancer potential of curcumin-loaded Ag–TiO_2-halloysite nanotubes (curcumin-loaded Ag–TiO_2-HNTs) was examined. Ag–TiO_2-HNTs with different wt% of Ag–TiO_2 were synthesized and characterized using XRD, TGA, FT-IR, UV-Vis spectroscopy, and SEM-EDX. The XRD results revealed the presence of crystalline TiO_2. However, the presence of Ag was detected through the SEM-EDX analysis. Cyclic voltammetry measurements suggested the enhancement of the release of ROS from TiO_2 upon deposition with Ag. FT-IR and TGA analysis confirmed the successful loading of curcumin inside the nanotubes of the halloysite. *In vitro* drug released studies revealed the release of approximately 80–99% curcumin within 48 hours. Kinetic model studies revealed that the release of curcumin from HNT and Ag–TiO_2-HNT followed the first-order and Higuchi models, respectively. The light irradiated curcumin-loaded Ag–TiO_2-HNTs samples exhibited considerable anticancer potential as compared to the free curcumin, irradiated Ag–TiO_2 NPs samples, and unirradiated curcumin loaded Ag–TiO_2-HNTs samples. The obtained results revealed that combined chemo- and photodynamic therapy using curcumin-loaded Ag–TiO_2-HNTs nanomaterial has the potential as an effective anticancer treatment method.

1 Introduction

In 2016, roughly one-third (~15.2 million) of all fatalities from noncommunicable diseases (NCDs) occurred among people between the ages of 30 to 69 years old. Out of this number of deaths, 40.8%, 29.8%, 7.0%, and 4.5% resulted from cardiovascular, cancer, chronic respiratory disorders, and diabetes, respectively. Although the mortality rate from cancer, in particular, is declining in most higher-income countries, this advancement cannot be said about lower-income countries in Sub-Saharan Africa.[1] In a quick response to tackle this major threat on sustainable human development and to curb the rapid rise in cancer related deaths in Sub-Saharan Africa and the world, several researchers in the past decades have been searching for anticancer drugs that is efficient, cost effective and easily available.

The most common therapeutic procedures in recent times for cancer treatment include immunotherapy, chemotherapy, radiation therapy, and surgery. Of all these procedures, chemotherapy remains one of the most effective and potent systems in tackling this canker.[2,3] Despite substantial progress in the discovery of efficient chemotherapy agents, their toxicity to normal tissues, adverse side effects in numerous organ systems, and drug resistance have remained serious setbacks.[4–6] Due to these setbacks, attempts in the last two decades have been made to better understand the molecular dynamics of some organic products that can be used to treat cancer in the context of modern medicine.[7]

Most of the natural products that have been experimentally examined so far have been confirmed to be harmless. Notable among them are curcumin,[8] irinotecan, vincristine, etoposide, and paclitaxel from plants, actinomycin D and mitomycin C from bacteria as well as marine-derived bleomycin.[9] Curcumin possesses anti-inflammatory, antioxidative and anticancerous activities which enables it to inhibit tumor cell proliferation.[8,10,11] Despite its efficacy and safety, low solubility in water and bioavailability have been highlighted as major problems. Low intrinsic activity, poor absorption, rapid metabolism, metabolic product inactivity, and rapid elimination from the body are all variables that contribute to its low bioavailability.[12] These aforementioned problems can however be overcome by

[a]*Department of Materials Science and Engineering, University of Ghana, LG 77, Legon-Accra, Ghana. E-mail: enyankson@ug.edu.gh*

[b]*Department of Biomedical Engineering, University of Ghana, LG 77, Legon-Accra, Ghana*

[c]*Department Biochemistry, Cell and Molecular Biology, University of Ghana, P.O. Box LG54, Legon, Ghana*

† Electronic supplementary information (ESI) available. See DOI: https://doi.org/10.1039/d2ra05777h

employing some formulations such as adjuvants, nanoparticles, liposomes, micelles, and phospholipids.[13]

However, in recent times, a lot of interest has been focused on naturally occurring nanostructured material such as halloysite nanotubes (HNTs).[13] HNTs ($Al_2Si_2O_5(OH)_4 \cdot nH_2O$) is a naturally occurring aluminosilicate material with unique combination of hollow tubular structure, large aspect ratio, and good mechanical strength. The outer layer which consists of tetrahedral siloxane (Si–O–Si) groups is negatively charged whiles the inner surface which is composed of octahedral aluminol (Al–OH) groups is positively charged. This unique combination gives it a broad potential in terms of functionality, that is, it allows for different modification approaches by immobilizing two or more materials with different functional groups at the same time.[14,15] Lastly, it is biocompatible, readily available, and low cost. These excellent properties make HNTs a possible drug carrier.[16–18]

One major limitation of chemotherapy drugs is that tumours easily develop resistance to such drugs. This results in metastasis. Studies have reported that development of drug resistance is multi-faceted in nature and therefore a therapy that employs multiple mechanism to kill cancer cells is required.[19] Although curcumin loaded HNTs has been investigated to suppress the proliferation of cancerous cell,[20] this research seeks to combine it with photodynamic therapy (PDT) in the treatment of cancerous cell. Photodynamic therapy (PDT) is a two-stage treatment method which involves the use of light radiation of a certain wavelength and drug (known as photosensitizer (PS)). This leads to the production of reactive oxygen species (ROS) such as singlet oxygen ($^1O_2$), hydroxyl radicals ($^{\bullet}OH$), hydrogen peroxide (H_2O_2) and superoxide anions ($O_2^{\bullet -}$), which have the ability to kill tumor cells.[21,22]

PDT can also be used to treat infections produced by bacteria, fungi, and viruses. Light-based therapy has also been observed to activate the immune system, offering the body another tool to fight malignant and precancerous cells, according to numerous studies.[23] PDT when applied have better advantage over chemotherapy because the ROS released will only attack in the light irradiation area since it has better spatial selectivity and invasiveness. This property reduces the toxicity level of PDT.[21]

Several different photosensitizing compounds such as porphyrin, chlorin, hypericin, phthalocyanine derivatives and acridine have been used over the years. Despite their numerous benefits, commonly used photosensitizers (PSs) have obstacles in their broad implementation in medicine. For example, most PSs are highly conjugated compounds with low water solubility or significant aggregation abilities in aqueous solutions, both of which result in low photodynamic activity.[22,24]

In recent times, the development of PDT has focused on the search for novel photosensitizers and specific carriers for their delivery, of which nanoparticles turn to lead in this selectivity.[25] Based on these studies, this research will pay particular attention to metallic and metal oxide nanoparticles (NPs), such as silver (Ag) and titanium dioxide (TiO_2) nanoparticles, respectively. TiO_2 NPs are frequently used in biomedical applications as result of its biocompatibility, photocatalytic efficiency and low cost.[26,27]

Since TiO_2 breakthrough in 1980s,[28] the photocatalytic efficacy of TiO_2 NPs has been thoroughly explored and it has been reported to show great potentials in its applications such as in solar energy, environmental remediation and photodynamic treatment. But its application in PDT still has major shortcomings due to it large band gap (3.2 eV for anatase) which limits its absorption of light to UV region of the electromagnetic spectrum. In addition, the photocatalytic efficiency of TiO_2 NPs is reduced due to the high rate of electrons–holes (e^-/h^+) recombination.[27,29] Despite these setbacks, TiO_2 has been reported to be the most efficient photosensitizer when compared to others due to its smaller size and anti-photodegradable stability.[30]

Metallic materials such as Pt, Au, Pd, Rh, Ni, Cu, and Ag nanoparticles can be coated onto TiO_2 NPs to improve their photocatalytic activity.[31] This study focuses on coating TiO_2 NPs with Ag NPs, due to its ready availability and low cost. Also, Ag NPs has dual functional sites, firstly, since its Fermi level is below the conduction band of TiO_2, Ag NPs function as an electron scavenging centre to separate e^-/h^+. Secondly, Ag NPs can trigger the surface plasmon resonance (SPR) effect in TiO_2 NPs, resulting in TiO_2 NPs having significantly increased photocatalytic activity in the visible range.[27,32,33]

TiO_2 NPs coated with Ag NPs used as a photosensitiser during photodynamic therapy has been reported by many studies to have an effective photocatalytic activity against different cancer cells[25–27,34–37] and curcumin also has been reported by numerous studies of suppressing the proliferation of cancerous cell.[3,8] Therefore, based on the evidence of these compounds exhibiting remarkable anticancer activities, this study examines the synergy between the anticancer effect of curcumin and Ag–TiO_2. This paper, therefore, reports the result of an investigation conducted into the potential application of combined curcumin and Ag–TiO_2-HNT platform as a vehicle for effective cancer treatment.

2 Experimental procedure

2.1 Materials and reagent

Curcumin (99% purity), halloysite nanotubes ($Al_2Si_2O_5(OH)_4 \cdot 2H_2O$) (99.5% purity), silver nitrate ($AgNO_3$) (>99.0% titration), and titanium(IV) oxide (mixture of rutile and anatase-TiO_2 with particle size ~ <100 nm) were purchased from Sigma-Aldrich (Gillingham, UK). Trypan Blue Solution (0.4% in phosphate-buffered saline (PBS)), fetal bovine serum (FBS), Dulbecco's modified Eagle's Medium (DMEM), penicillin/streptomycin, MTT (3-(4,5-dimethyl-thiazol-2-yl)-2,5-diphenyl-tetrazolium bromide) were obtained from the Biochemistry Department Lab, University of Ghana. Phosphate-buffered saline and ethanol were also purchased from Sigma Aldrich (Gillingham, UK).

2.2 Synthesis of Ag–TiO_2 and Ag–TiO_2-halloysite nanomaterial (Ag–TiO_2-HNTs)

1 g of TiO_2 was first dispersed in 200 mL of distilled water while stirring. This was labelled as solution A. Again, a specific amount of silver nitrate ($AgNO_3$) corresponding to 0.5, 1.5 and 3

wt% was also dissolved in 50 mL of absolute ethanol. This was labelled as solution B. Solution A and B were then combined, and the resulting solution was continuously stirred in the dark for 1 hour. This was then transferred to a photo reactor for UV illumination for 2 hours. After two hours of UV light irradiation, the color of the mixture changed from white to dark brown depicting the formation of silver nanoparticles. The mixture was then centrifuged at 2300 rpm for 15 min to obtain the Ag–TiO_2 nanoparticles. The particles were washed several times with ethanol–water mixture to get rid of excess $AgNO_3$ and dried at 105 °C for 5 hours. The obtained particles were grinded and sieved with 75 micrometer sieves.

For the Ag–TiO_2-HNT nanomaterial, 1 g of TiO_2 was first dispersed in 200 mL of distilled water while stirring. This was labelled as solution A. Again, a specific amount of silver nitrate corresponding to 0.5, 1.5, and 3 wt% was also dissolved in 50 mL of absolute ethanol. This solution was labelled as solution B. Solutions A and B were then combined, and the resulting solution was continuously stirred in the dark for 1 hour. This was then transferred to a photo reactor for UV illumination for 2 hours. After the illumination process with accompanying color change, an amount of HNTs already dispersed in 50 mL of distilled water was added to mixture. Different wt% of HNTs were used to obtain Ag–TiO_2-HNT nanomaterial with 10, 30, and 50 wt% TiO_2. The Ag–TiO_2-HNT mixture was again stirred in the dark for 1 hour after which it was centrifuged for 15 min, sonicated with 10 mL of absolute ethanol for 30 min, and finally oven dried at 105 °C for 5 hours. Finally, the Ag–TiO_2-HNT sample obtained was grinded and sieved with 75 micrometer sieves.

2.3 Loading of the curcumin on Ag–TiO_2-halloysite nanomaterial

The entrapment method used in this study is a modified form of a procedure reported by Price *et al.*[38] First, 26 mg of curcumin was dissolved in 4 mL of ethanol to obtain 6.5 mg mL^{-1} saturated solution. Then, 200 mg of the Ag–TiO_2-HNT-nanomaterial was dispersed in 1.5 mL of the 6.5 mg mL^{-1} curcumin saturated solution. The obtained mixture was then sonicated for 15 min and transferred into a vacuum jar and vacuum applied for 30 min with the vacuum broken at every 10 min. The process was then repeated twice to ensure that the Ag–TiO_2-HNT nanomaterial was filled with maximum amount of the curcumin. The obtained composite was then washed with distilled water and absolute ethanol (water/ethanol 50% v/v) and centrifuged at 6000 rpm for 20 min to remove excess curcumin. The obtained particles were finally dried under vacuum for 2 hours to obtain curcumin loaded Ag–TiO_2-HNTs nanomaterial.

2.4 Characterization

XRD was conducted to examine the phases present in the samples synthesized. CuKα x-rays with a wavelength of 0.15406 nm was utilized at a 2θ range of 5.0525 to 99.8675° with 0.1050° step size.

The optical properties of the synthesized samples were examined using UV-vis spectroscopy. In this studies, 10 mg of the sample dispersed in 40 mL of distil water was used for the UV-vis analysis. This analysis was conducted using Genesys UV-vis spectrophotometer.

The thermal stability of the samples was examined using thermogravimetric analysis (TGA). The samples were heated from room temperature to 800 °C at a heating rate of 10 °C min^{-1} in Nitrogen gas atmosphere.

Thermo Scientific™ Nicolet™ iS™ 10 Fourier transform infrared spectroscopy (FTIR) was utilized to examine the functional groups present in the synthesized samples. The analysis was done from 500 to 4000 cm^{-1}.

The cyclic voltammetry (CV) measurements were performed with an electrochemical workstation connected to a desktop to examine the production of ROS by the samples. 2 mg each of TiO_2 NPs, Ag–TiO_2 NPs and Ag–TiO_2-HNTs samples were dispersed separately in 1 mL of distilled water to obtain concentration of 2 mg mL^{-1}. These were then irradiated with light. 5 μl of each of these aqueous samples were then used for the electrochemical performance at room temperature using Ag/AgCl as a reference electrode.

2.5 Drug release analysis

The regular dialysis bag method was used to investigate the *in vitro* release of free curcumin from loaded Ag–TiO_2-HNTs nanomaterial. Phosphate-buffered saline (PBS at a pH of 7.4) and ethanol (50% v/v) was used as the medium. 40 mg of the curcumin loaded Ag–TiO_2-HNT composite and 1 mL of the medium were introduced into the bag. This was then transferred to a beaker filled with 100 mL of the same media and was kept at 37 °C with gentle agitation. At every 2 hours, 2 mL of the medium in the beaker was withdrawn and replaced with 2 mL of the same medium (fresh) to maintain sink conditions. The set-up was carefully shielded from light. The amount of curcumin released at specific time intervals were examined using UV spectroscopy measurement at a wavelength of 430 nm. The experiment was conducted in triplicate and the average was reported.

2.6 Sample activation

First, 2 mg each of TiO_2 NPs, Ag–TiO_2 NPs and HNTs-Ag–TiO_2 samples were dispersed separately in 1 mL of distil water to obtain concentration of 2 mg mL^{-1}. These were then exposed to a germicidal UV lamp for 2 hours for the TiO_2 and Ag–TiO_2 NPs samples and 5 hours for the HNTs-Ag–TiO_2 and Curcumin loaded HNTs-Ag–TiO_2 nanomaterial samples. After irradiation, the relative cytotoxicities of both irradiated and unirradiated TiO_2 NPs, Ag–TiO_2 NPs, HNTs-Ag–TiO_2 and Curcumin loaded HNTs-Ag–TiO_2 against HeLa cells were assessed using MTT assays after 48 hours.

2.7 Testing of the drug loaded nanomaterials on HeLa cells (cancer cells)

2.7.1 Cell line and culture conditions. The HeLa cell line was maintained in Dulbecco's Modified Eagle Medium (DMEM) supplemented with 10% fetal bovine serum (FBS) and 1%, penicillin (100 U mL^{-1}) streptomycin (100 U mL^{-1}). Cells were

cultured at 37 °C in 5% CO_2 incubator till they reached the exponential phase. The medium was then discarded from the adherent cells, washed with 1x PBS and 1x Trypsin-EDTA added to detach cells from flask. The detached cells in the medium were centrifuged for five minutes at 1100 rpm and the supernatant was discarded and resuspend in 1 mL media.

2.7.2 Trypan blue exclusion assay. 20 μL of the resuspended media was added to 20 μL of trypan blue and counted using the hemocytometer under a light microscope. Cell viability (CV) was calculated for each treatment using eqn (1)

$$\text{Cell viability percent(CV\%)} = \frac{\text{NS}_{\text{cells}}}{\text{S}_{\text{cells}}\,\text{XNS}_{\text{cells}}} \times 100\% \quad (1)$$

where S_{cells} and NS_{cells} were the counted cells that had or not taken up the dye.

2.7.3 MTT assay. To test the effect of the nanomaterial samples on cancer cells, an MTT colorimetric assay was used. This test is based on the ability of living cells to convert MTT (3-(4,5-dimethyl-thiazol-2-yl)-2,5-diphenyl-tetrazolium bromide), a yellow soluble salt, to a purple-blue insoluble formazan precipitate. 10 000 cells per well were seeded in triplicate in a 96-well plate and kept in an incubator for 24 hours. After 24 hours, the seeded cells were treated with various concentration of the drug and incubated for 48 hours. The concentration of the drug ranged from 20 to 100 μg mL^{-1}. When the incubation period was over, 20 μL of 2.5 mg mL^{-1} of MTT in PBS (0.5 mg mL^{-1}) was added to each well and incubated for another 4 hours. After the 4 hours, the reaction was stopped using 100 μL per well of acidified isopropanol and then placed on orbital shaker for 15 minutes. Changes in absorbance at 570 nm were recorded using a plate reader spectrophotometer to determine the amount of formazan (which was directly related to the number of live cells). The cell viability was calculated from eqn (2).

$$\text{Cell viability percent(CV\%)} = \frac{\text{absorbance of the test} - \text{absorbance of the colour control}}{\text{absorbance of the negative control} - \text{absorbance of blank}} \times 100\% \quad (2)$$

where, blank denotes media only, colour control denotes media and drug, negative control denotes cells and media and test denotes cells, media and drug.

The cell viability text was conducted in triplicates and the data were shown by mean ± SD.

3 Results and discussion

3.1 XRD analysis

The phases present in the samples were determined using XRD analysis and presented in Fig. 1. The XRD pattern of the TiO_2 revealed the presence of both the anatase and rutile phases. The anatase phases were observed at 2 theta positions of 25.5, 38.0, 48.2, 54.0, 55.2, 69.0, 70.5, 75.2, 76.2, 82.8° representing the crystallographic planes (101), (004), (200), (105), (211), (116), (220), (215), (301) and (224), respectively. This corresponds to the JCPDS File no. 21-1272. On the other hand, the rutile phases were identified at 2 theta positions of 27.6 and 62.9° representing the crystallographic planes (110) and (002), respectively. This corresponds to JCPDS File no. 21-1276 standard. The 2 theta positions of the HNT peaks were observed at 11.9, 20.0, 24.9, 26.7 and 30.3°, respectively representing (001), (020), (002), (130) and (132) crystallographic planes. This corresponds to JCPSD File no. 29-148 standard.

In Fig. 1(b), no notable peak of Ag was observed. The silver in the composite material was too small to be detected by XRD technique. Similar observation has been reported in literature.[39] The TiO_2 and HNT characteristic peaks were however observed in the XRD patterns of the TiO_2–Ag-HNT nanomaterial, implying that the nanomaterial formed contained TiO_2 and HNTs.

Debye–Scherrer Method and Williamson–Hall Method (W–H method) presented in eqn (3) and (4), respectively were employed to estimate the average crystallite size of the Ag–TiO_2 samples. In using the Debye–Scherrer method, the average crystallite size (D) are determined by using the Full Width at Half Maximum (FWHM) of the three (3) most intense peaks.[40]

$$D = \frac{0.9\lambda}{\beta \cos\theta} \quad (3)$$

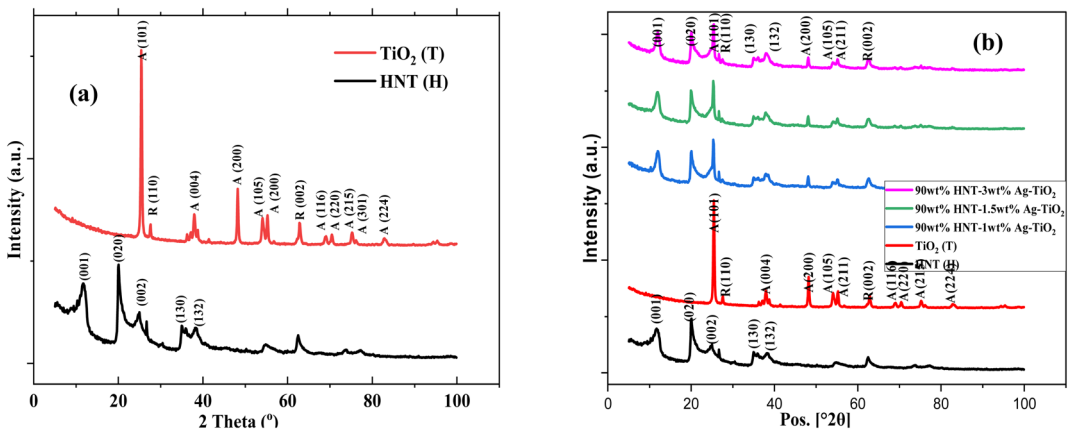

Fig. 1 XRD pattern of (a) Halloysite Nanotubes (HNT) and TiO_2, and (b) HNT, TiO_2 and TiO_2–Ag-HNT nanomaterials.

Table 1 The average crystallite size (D), lattice strain, lattice parameters (a, b and c) for TiO_2 and Ag–TiO_2

Sample	Silver content	Crystallite size by Scherrer (nm)	Crystallite size by W–H plot (nm)	Strain (ε) $\times 10^3$	Lattice parameter(Å)	
					Anatase; $a = b$	Rutile; $a = b$
TiO_2	0 wt%	26.573	32.32	1.16	$a = 3.7754$ $c = 9.48036$	$a = 4.5737$ $c = 2.95652$
TiO_2-1 wt% Ag	1 wt%	26.554	32.93	1.06	$a = 3.7818$ $c = 9.50336$	$a = 4.5871$ $c = 2.95942$
TiO_2-1.5 wt% Ag	1.5 wt%	24.321	30.03	1.15	$a = 3.78126$ $c = 9.4938$	$a = 4.5866$ $c = 2.95878$
TiO_2-3 wt% Ag	3 wt%	24.320	30.01	1.16	$a = 3.78244$ $c = 9.49804$	$a = 4.5874$ $c = 2.95978$

where D, θ, 0.9, β and λ are the average crystallite size, angle of diffraction, shape factor (spherical), full width at half maximum and wavelength of X-ray radiation (Cu Kα = 1.5406 Å), respectively. Similarly, the average crystallite size and strain were calculated using the Williamson–Hall method represented in eqn (4) below.[40]

$$\beta \cos \theta = \frac{0.9\lambda}{D} + 4\varepsilon \sin \theta \quad (4)$$

where ε is induced strain in crystallite and the rest of the parameters have the same meaning as in eqn (3). The parameters calculated from these models are presented in Table 1.

As shown in Table 1, the average crystallite sizes obtained from the Scherrer method was relatively smaller than those obtained from the W–H method. It should be noted that, for the same method, the crystallite sizes showed a little be dissimilarities for all the samples. One notable observation is that the crystallite sizes and strain relatively decreased with increasing wt% of Ag. According to the W–H technique, the strain caused by Ag inclusion in TiO_2 lattice can lead to the XRD line broadening, which result in the reduction of the crystallite size.[40,41] In addition, the lattice parameters obtained for the anatase phase showed slight changes for all the samples. A similar observation was made for the lattice parameters of the rutile phase.

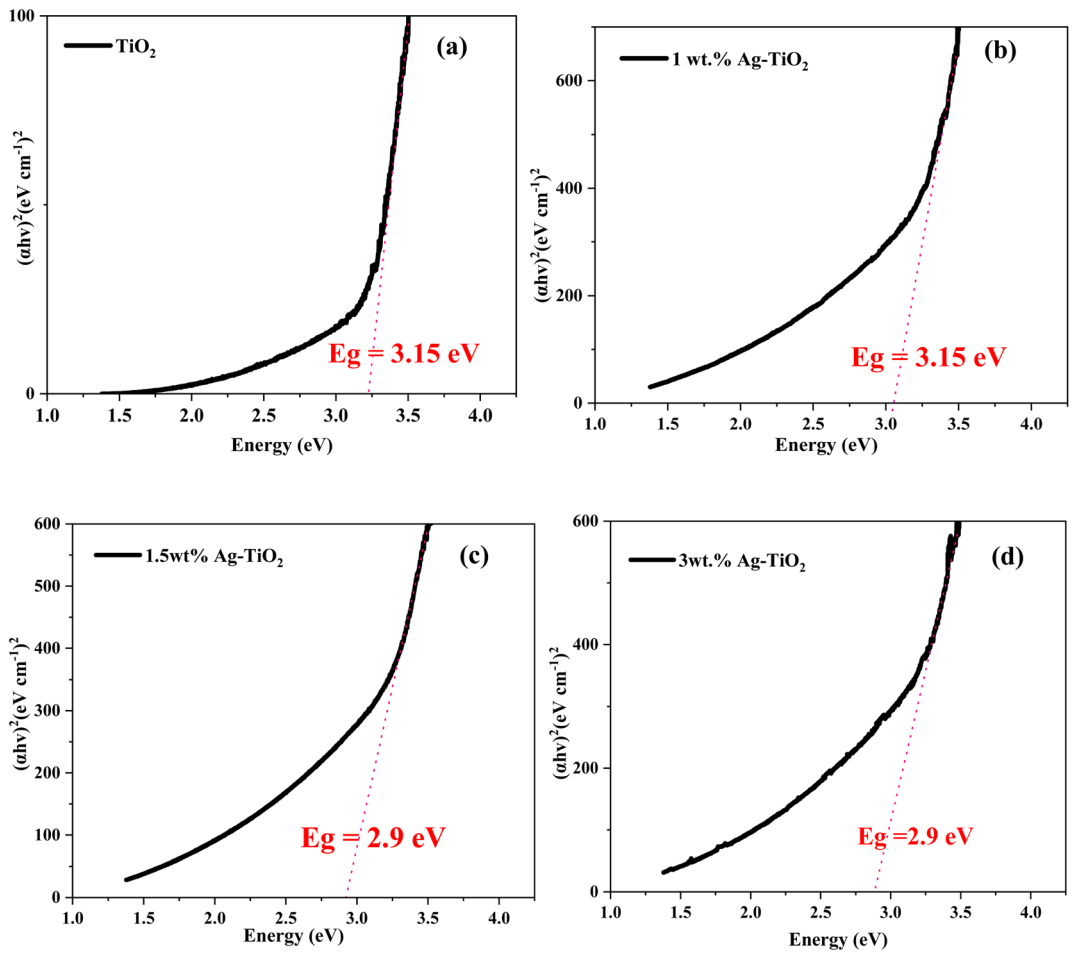

Fig. 2 Tauc plots of (a) TiO_2 (b)1 wt% Ag–TiO_2, (c) 1.5 wt% Ag–TiO_2 and (d) 3 wt% Ag–TiO_2.

3.2 Optical band gap estimation

Tauc Davis–Mott relation depicted in eqn (5) was used to determine the optical band gap energy of the samples.[42]

$$\alpha h\nu = A(h\nu - E_g)^m \quad (5)$$

where α is the absorption coefficient, h and ν are Planck constant and photon frequency ($h\nu$ = photon energy), respectively, A is a constant, E_g is the optical band gap, and m is equal to 1/2 for authorized direct optical transitions. The band gap values were calculated by the linear section of the plot shown in Fig. 2 and the band gap value of each sample was determined by setting hν = 0. From the Tauc plots of $(\alpha h\nu)^2$ *versus* $h\nu$, the direct band gap values estimated are presented in Fig. 2. The Tauc plots and the estimated optical band gap of the other samples are presented in Fig. 1S in the ESI.†

The band gap energy of the TiO_2 NPs decreases with increasing content of the Ag species as can be seen in Fig. 2. Halloysite serving as a support apparently plays a complex role *i.e.*, it may retard recombination of separated charges generated by UV light irradiation in the crystal lattice of TiO_2, thereby increasing catalytic activity. Conversely, halloysite may have a shielding effect, *i.e.* through scattering or absorbing a certain percentage of the incoming UV light irradiation, decreasing the catalytic activity.[43] From Fig. 1S in the ESI,† upon the addition of halloysite to the Ag–TiO_2 NPs, in our case a decreased in optical band gap was observed, suggesting that the shielding effect is not significant. This implies that the HNT-Ag–TiO_2 nanomaterial is highly effective for photocatalytic material.

3.3 Scanning electron microcopy-energy dispersive X-ray spectroscopy (SEM-EDX)

SEM-EDX was utilized to examine the morphology and elemental composition of the synthesized samples. The SEM-EDX images are presented in Fig. 3. The tubular and the spherical morphology of halloysite nanotubes and TiO_2, respectively are clearly visible in the SEM images provided in Fig. 3(a). The SEM images of the Ag–TiO_2-HNT showed significant agglomeration. Upon loading with curcumin (Fig. 3(b)), no difference in the morphology was observed. The sample also showed significant agglomeration. The SEM-EDX (Fig. 3(c))

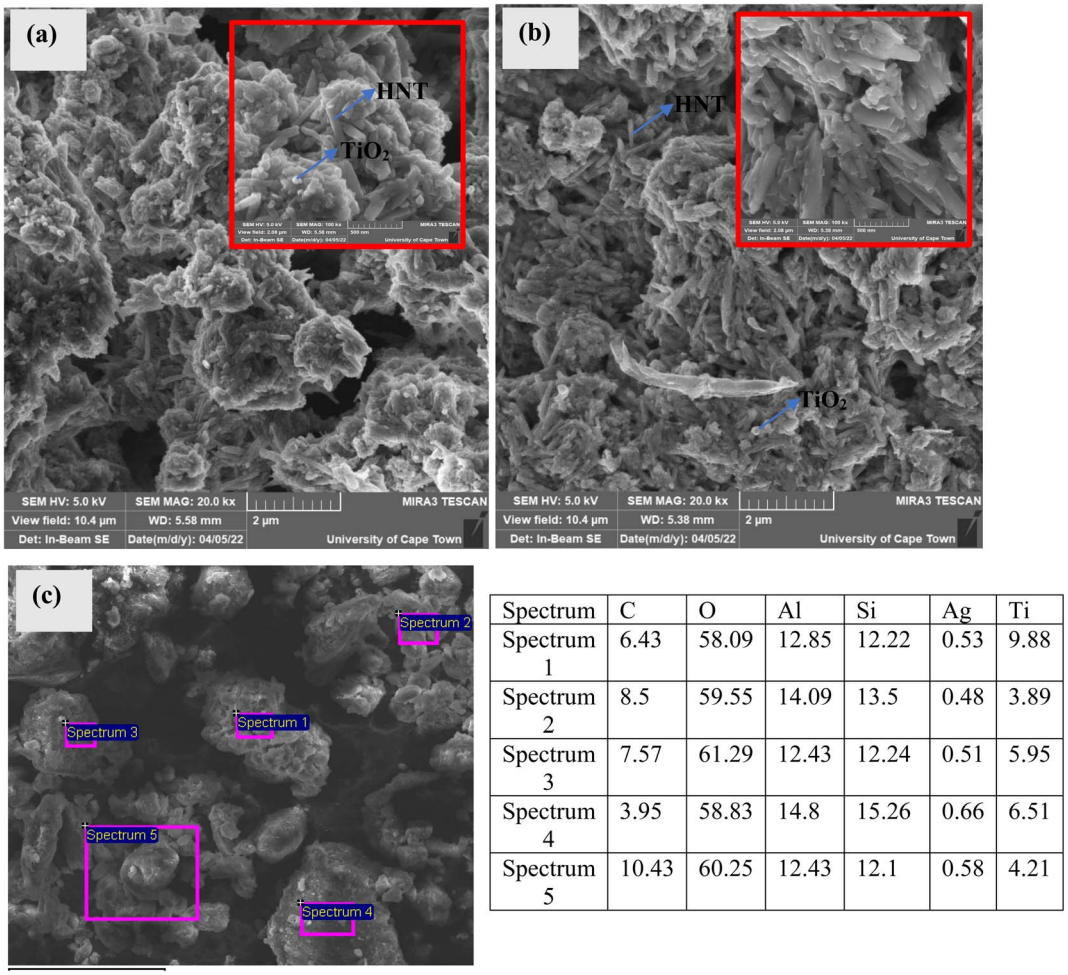

Spectrum	C	O	Al	Si	Ag	Ti
Spectrum 1	6.43	58.09	12.85	12.22	0.53	9.88
Spectrum 2	8.5	59.55	14.09	13.5	0.48	3.89
Spectrum 3	7.57	61.29	12.43	12.24	0.51	5.95
Spectrum 4	3.95	58.83	14.8	15.26	0.66	6.51
Spectrum 5	10.43	60.25	12.43	12.1	0.58	4.21

Fig. 3 SEM images of (a) 1.5 wt% Ag–TiO_2-90 wt% HNT [high magnification image inserted], (b) curcumin loaded 1.5 wt% Ag–TiO_2-90 wt% HNT [high magnification image inserted], (c) EDX image of Curcumin loaded 1.5 wt% Ag–TiO_2-90 wt% HNT and table presenting the elements identified in the samples with their corresponding weight percentages.

analysis of the curcumin loaded Ag–TiO_2-HNT detected Ag, Ti, Al, Si, O and C which confirmed the presence of Ag, TiO_2, HNTs and curcumin. It should however be mentioned that the C may also be from the carbon tape used for the SEM analysis.

3.4 FTIR analysis

FTIR analysis was conducted to further examine the presence of the functional groups in the composite and to confirm the loading of curcumin into the nanomaterial. The FTIR spectra are presented in Fig. 4. For the IR spectrum of curcumin shown in Fig. 4(a), the stretching vibrations at 3509 cm^{-1} is related to phenolic O–H vibrations, whereas the stretching vibrations at 1507 and 1629 cm^{-1} are connected with the carbonyl (C=O) and alkenes (C=C) character, respectively. Finally the C–O–C stretching vibration and C–H bending vibrations are represented by the peaks found at 1277 cm^{-1} and 1428 cm^{-1}, respectively.[20,44] The FTIR spectrum of TiO_2 is also shown in Fig. 4(a). The peaks at 3903, 3751, and 3629 cm^{-1} in the spectrum of TiO_2 are related to the O–H stretching vibration. The bending vibrations of the absorbed water molecules are represented by the bands at 1742 and 1215 cm^{-1}. The broad band between 450 and 850 cm^{-1} corresponds to the Ti–O bending mode of vibrations, which indicates the presence of metal oxygen bonding.[45,46] The FT-IR spectrum of HNTs (H) as shown in Fig. 4(a) also reveals double peaks at 3692 and 3621 cm^{-1}, which are attributable to the stretching vibrations of inner-surface hydroxyl groups. The deformation vibration at 1742 cm^{-1} indicates interlayer water. The Si–O network vibration modes were associated with the peak at 1030 cm^{-1}. The band recorded at 532 cm^{-1} is deformation vibration of Al–O–Si, while the hydroxy bending vibration absorption peak occurred at 912 cm^{-1}.[47–50]

The FTIR spectra of Ag–TiO_2 samples are represented in Fig. 4(b). When compared to TiO_2, the Ag–TiO_2 showed nearly identical bands, however the spectrum intensive peaks fell marginally as silver content increased. The spectra of Ag–TiO_2-HNTs nanomaterial samples are shown in Fig. 4(c). The nanomaterial spectra exhibited characteristic bands of both HNTs and TiO_2 confirming the formation of Ag–TiO_2-HNTs nanomaterial samples. None of the characteristic bands of the nanomaterial were affected except the Si–O network vibration modes that appeared at about 1030 cm^{-1} for the HNTs which shifted for all the nanomaterials to about 1024, 1025 and 1023 cm^{-1}. The shifting of the Si–O network vibration modes indicates an interaction between TiO_2 and the outer surfaces of HNTs.[43,51]

The spectra of the curcumin loaded Ag–TiO_2-HNTs nanomaterial samples are shown in Fig. 4(d). Some of the peaks

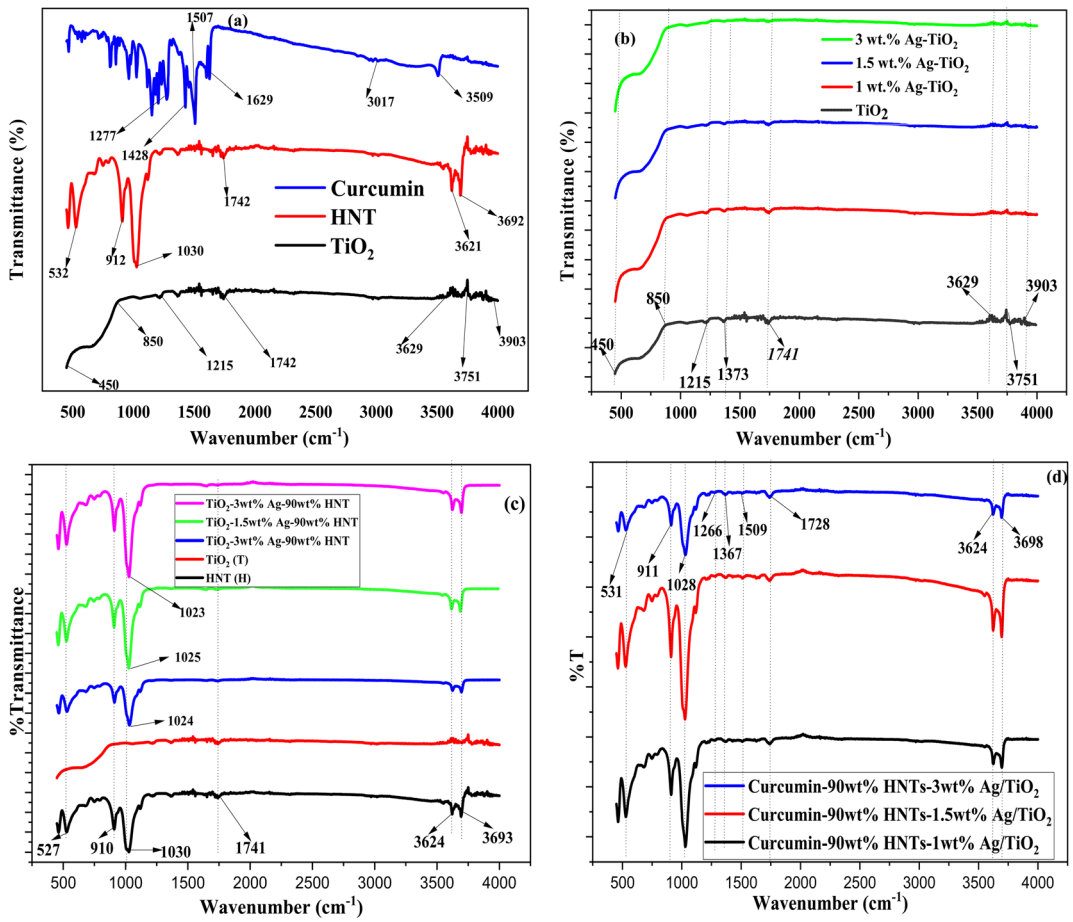

Fig. 4 FTIR of (a) curcumin, HNT and TiO_2 (b) TiO_2 and Ag–TiO_2 (c) HNT, TiO_2 and Ag–TiO_2-HNT and (d) curcumin loaded Ag–TiO_2-HNT.

slightly shifted to higher wavenumbers. In addition, the hydroxyl peaks present in curcumin were overshadowed by the hydroxyl bands of HNTs.

3.5 Thermogravimetric analysis (TGA)

TGA analysis were performed to confirm the successful loading of curcumin into the nanotubes of the halloysite. As shown in Fig. 5(a and c), the TGA curves generated some decomposition steps. In all these curves, decomposition of adsorbed water molecules on the surface of all the samples were observed from 20–100 °C. This initial stage of decomposition for all the samples were due to evaporation of the adsorbed water molecules at *ca.* 100 °C. The TGA curves for HNT and curcumin loaded HNT as shown in Fig. 5(a), went through decomposition from *ca.* 100–800 °C with their total weight losses presented in Table 1S in the ESI.† Between 20–100 °C, HNTs and Curcumin loaded HNTs recorded 4.5 and 3.3% weight loss, respectively. From Fig. 5(b), significant amount of this loss occurred at *ca.* 40 °C for both samples. Between 100 and 800 °C, *ca.* 15.6% and 19.5% of weight loss was recorded by HNTs and curcumin loaded HNTs, respectively. From Fig. 5(b), a significant amount of these weight losses occurred at exactly 470 °C and 485 °C, for HNTs and curcumin loaded HNTs, respectively. These weight losses can be attributed to the dihydroxylation of HNTs[52,53] and the decomposition of curcumin.[54]

The synthesized Ag–TiO_2-HNT nanomaterial loaded with curcumin also underwent various stages of decomposition between 100–800 °C as illustrated in Fig. 5(c) and their corresponding total weight losses are also summarized in Table 1S in the ESI.† From Fig. 5(b), as already stated, the main weight loss for HNT and curcumin loaded HNT occurred at *ca.* 470 and 485 °C, respectively. However, for the nanomaterials and curcumin loaded nanomaterials, the significant weight losses recorded were at *ca.* 465–470 °C and 475–482 °C, respectively. As illustrated in Table 1S,† the percentage of curcumin content measured by the TGA confirm the successful loading of the curcumin in the nanotubes of the halloysite. These results affirm the FTIR and SEM-EDX findings. From the TGA analysis, the amount of curcumin loaded into the HNTs was *ca.* 3.9 wt%. For the Ag–TiO_2-HNTs composite, the amount of curcumin loaded increased with increasing amount HNTs in the

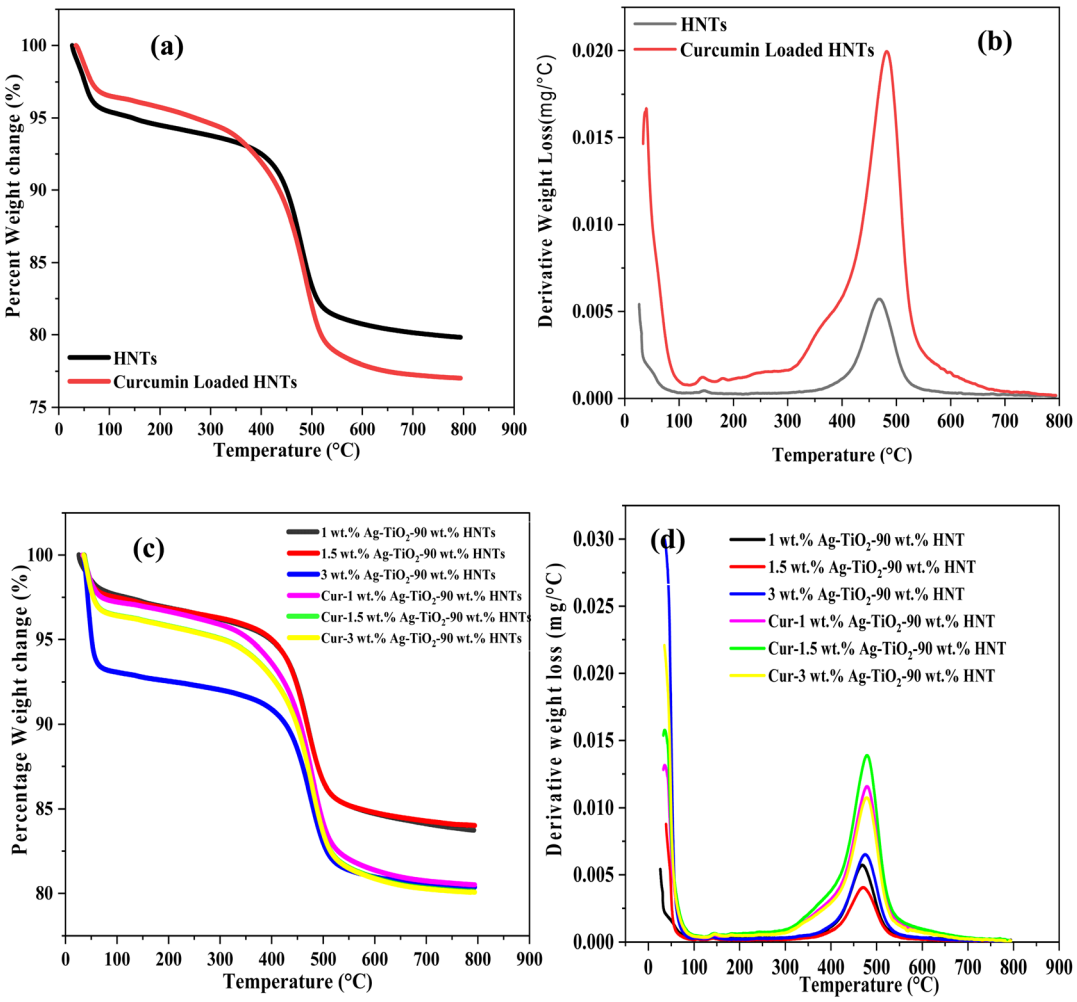

Fig. 5 (a) TGA of HNT and curcumin loaded HNTs (b) derivative weight loss of HNTs and curcumin loaded HNTs (c) TGA of Ag–TiO_2-HNTs and curcumin loaded Ag–TiO_2-HNT (d) derivate of weight loss of Ag–TiO_2-HNTs and curcumin loaded Ag–TiO_2-HNT.

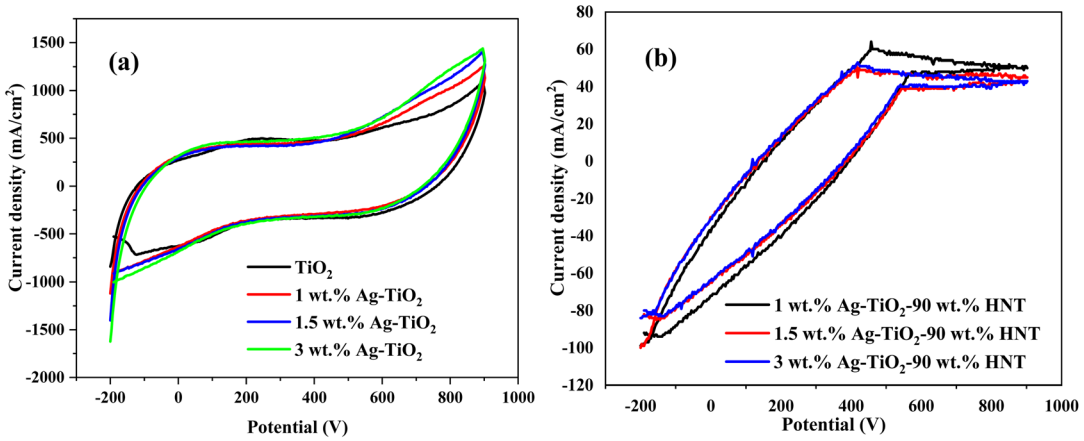

Fig. 6 Cyclic voltametric (CV) curves of (a) TiO_2 and Ag–TiO_2 (b) Ag–TiO_2-90 wt% HNT nanomaterials.

Table 2 Drug encapsulation efficiency (EE%) and loading efficiency (LE%) values of each loaded sample

Sample	Amount of Cur. in NPs (mg)	EE%	LE%
Cur-1 wt% Ag–TiO_2-90 wt% HNT	5.57	21.41	2.78
Cur-1.5 wt% Ag–TiO_2-90 wt% HNT	7.40	28.46	3.70
Cur-3 wt% Ag–TiO_2-90 wt% HNT	7.26	27.92	3.63
Curcumin-HNT	7.78	29.90	3.89

composite (Table 1S†). Generally, the amount of curcumin loaded into the composite varied from 1.7–3.6 wt%.

3.6 Cyclic voltammetry analysis

The essence of the electrochemical performance on the sample was to evaluate the rate of Reactive Oxygen Species (ROS) released as a function of time using light irradiation. This is necessary because for the application being examined, the release rate of ROS is very crucial. All the samples were subjected to 4 hours of irradiation. The cyclic voltammetry (CV) was carried out at a constant scan rate of 160 mV s^{-1} in the potential window of −200 to 0.9 mV (*vs.* Ag/AgCl) for all the samples under investigation. All the CV curves as shown in Fig. 6 represent a typical quasi-rectangular shape which resembles the electrochemical double-layer capacitor (EDLC). In comparison to the Ag–TiO_2 samples, the pure TiO_2, displayed a quasi-rectangular CV profile with the anodic peak current increasing marginally with the silver content. This implies that, all the samples did not induced resistance in the ionic flow at the same voltage, however each of them produces the ROS at different current as shown in Fig. 6(a). The high ions mobility of the Ag–TiO_2 samples was influenced by the Ag NPs content present. This implies that the silver content really influenced the ROS generation of the bare TiO_2. All the CV curves of the Ag–TiO_2-HNT nanomaterials as shown in Fig. 6(b), also followed the same characteristic pattern of Fig. 6(a). This implies that, the halloysite content presence does not influence the released of the ions.

3.7 Drug release study

The drug encapsulation efficiency (EE) and loading efficiency (LE) of the curcumin loaded Ag–TiO_2-HNTs samples were computed using eqn (6) and (7), respectively and the results are shown in Table 2.[55]

$$\mathrm{EE\%} = \frac{\text{total amount of drug in nanoparticles}}{\text{total amount of drug used for loading}} \times 100\% \quad (6)$$

$$\mathrm{LE\%} = \frac{\text{total amount of drug in nanoparticles}}{\text{total amount of nanoparticles}} \times 100\% \quad (7)$$

From Table 2, the approximated maximum encapsulation efficiency (EE%) was 28.50% for the Ag–TiO_2-HNT nanomaterial and 29.90% for the pure HNT. Again, the approximated maximum loading efficiency (LE%) for the nanomaterial was 3.7% whiles for the pure HNT, its loading efficiency (LE%) was ~3.9%.

The *in vitro* drug release from curcumin loaded HNTs and curcumin loaded Ag–TiO_2-HNTs nanomaterials were studied using PBS (pH 7.4) and ethanol (50% v/v) at a temperature of 37 °C. All release behaviour lasted for almost 48 hours. It can be observed in Fig. 7 that, the release percentages after 10 hours of free curcumin were below 50%. However, after 24 hours, the cumulative released percentage was above the 50% mark as illustrated in Table 2S.† After the 48 hours, the release percentages were above the 80% mark except for curcumin-90 wt% HNT-3 wt% Ag–TiO_2 sample. The highest release rate occurred was 81.7% which corresponds to the sample with less Ag content while the lowest release rate occurred at 51.9% corresponding to the sample with highest silver content. The released rate for HNT loaded with curcumin was also above the 80% mark after 48 hours. From all the released curves, the drug release rate was shown to decrease with increasing silver concentration. Since most of the dissolution indicated more than 80% of the drug released within the released time then it complies with the pharmacopoeia specifications.[56]

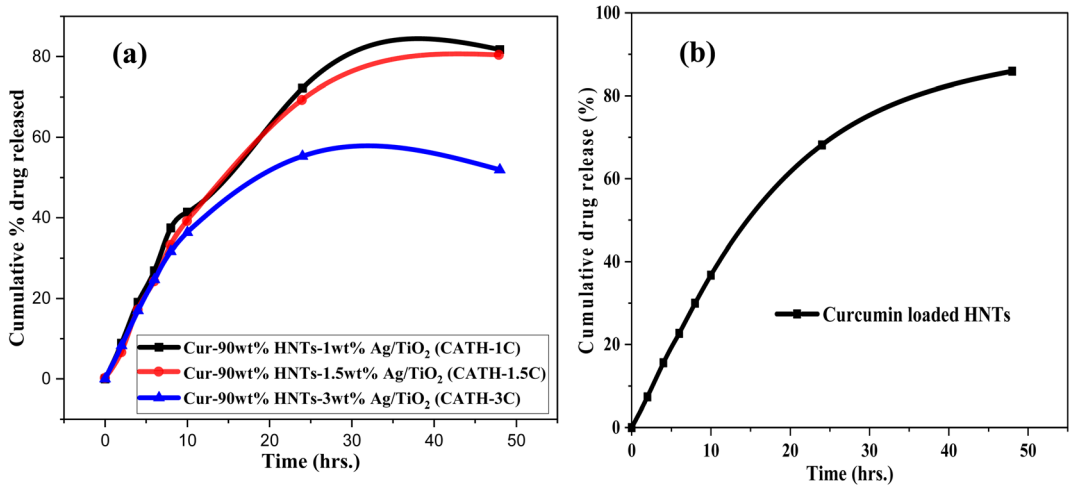

Fig. 7 Cumulative drug release (%) for (a) curcumin loaded Ag–TiO_2-HNTs (b) curcumin loaded HNTs.

Table 3 R^2 and rate constant values for the different kinetic models

Models	Parameters	Cur-1 wt% Ag–TiO_2-90 wt% HNTs	Cur-1.5 wt% Ag–TiO_2-90 wt% HNTs	Cur-3 wt% Ag–TiO_2-90 wt% HNTs	Cur-HNT
Zero-order $C_o - C_t = k_o t$	k_o	1.643	1.648	0.999	1.768
	R^2	0.833	0.855	0.663	0.906
First order $\log C = \log C_o - k_1 t/2.303$	k_1	0.02	0.02	0.01	0.02
	R^2	0.943	0.955	0.701	0.993
Higuchi $Q = k_H x t^{1/2}$	k_H	13.22	13.1	8.61	13.74
	R^2	0.956	0.958	0.874	0.970
Korsmeyer-Peppas $\log(M_t/M_\infty) = \log k_{kp} + n \log t$	k_{kp}	1.03	1.06	0.933	1.065
	R^2	0.837	0.871	0.788	0.884
	n	1.60	1.56	0.98	0.96
Hixon-Crowell ${W_0}^{1/3} - {W_t}^{1/3} = k_{HC} t$	k_{HC}	0.042	0.041	0.02	0.047
	R^2	0.913	0.928	0.696	0.974

3.8 Drug release kinetic study

Fitting the results of *in vitro* drug release investigations into well-known kinetic equations such as the zero-order model, first-order model, Higuchi model, Korsmeyer-Peppas model, and Hixson-Crowell model is vital for understanding the kinetics of drug release.[57] These models are represented graphically in Fig. 2S–6S in the ESI.† The summary of the rate constants and correlation coefficients (R^2) acquired from these models are reported in Table 3. The model that best fits the drug release kinetics is determined by the highest degree of correlation coefficient from the regression evaluation.

From Table 3 it can be observed that, for the curcumin-loaded halloysite sample, a higher correlation was recorded with the first-order ($R^2 = 0.993$) compared to the zero-order ($R^2 = 0.906$), Higuchi ($R^2 = 0.970$), Korsmeyer-Peppas ($R^2 = 0.884$), and Hixson-Crowell ($R^2 = 0.974$) models. For the curcumin released from the nanomaterials (1 wt% Ag–TiO_2-90 wt% HNTs, 1.5 wt% Ag–TiO_2-90 wt% HNTs and 3 wt% Ag–TiO_2-90 wt% HNTs), the higher correlation was displayed by the Higuchi model ($R^2 = 0.956$, 0.958 & 0.874) than the zero-order ($R^2 = 0.883$, 0.855 & 0.663), first-order ($R^2 = 0.943$, 0.935 & 0.701), Korsmeyer-Peppas ($R^2 = 0.837$, 0.871 & 0.788), and Hixson-Crowell ($R^2 = 0.913$, 0.924 & 0.696) models.

The release profiles for the curcumin loaded HNTs was best described by the first-order model while that of the nanomaterials was best described by the Higuchi model. The release of curcumin from the halloysite nanotubes is therefore characterized by the nanoporous structure of the HNTs. This is because, the first order model describes drug dissolution in pharmaceutical dosage forms such as those contained in a porous matrix.[57] For the curcumin loaded nanomaterials, the release profile follows the Higuchi model due to the heterogeneous nature of the nanomaterial. Thus, Higuchi model always describes the release profile of drugs from an insoluble matrix system.[57]

A zero-order release kinetics depicts a constant release rate of the drug from the halloysite nanotubes.[20] As can be seen in Fig. 7, the release rate of curcumin from the Ag–TiO_2-HNTs and HNTs were not constant implying that the release did not follow a zero-order kinetic model. It is therefore not surprising that the R^2 values obtained from the zero-order kinetic model were relatively lower compared to that of the Higuchi and first order kinetic models.

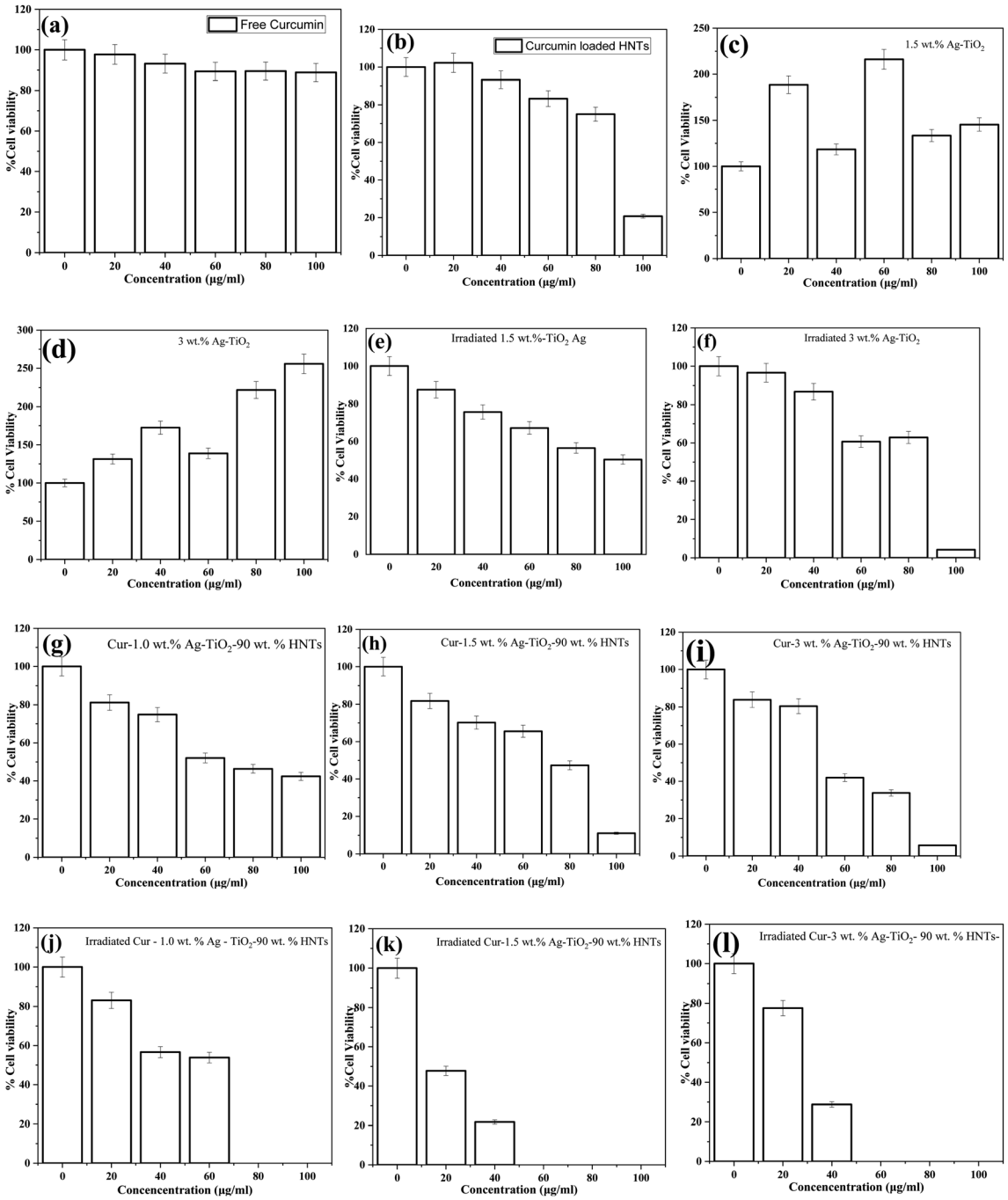

Fig. 8 The effect of the samples on the cell viability (a) free curcumin, (b) curcumin loaded HNTs, (c) inactivated 1.5 wt% Ag–TiO_2, (d) inactivated 3.0 wt% Ag–TiO_2, (e) irradiated 1.5 wt% Ag–TiO_2, (f) irradiated 3.0 wt% Ag–TiO_2, (g) Cur-1 wt% Ag–TiO_2-90 wt% HNTs, (h) Cur-1.5 wt% Ag–TiO_2-90 wt% HNTs, (i) Cur-3.0 wt% Ag–TiO_2-90 wt% HNTs, (j) irradiated Cur-1 wt% Ag–TiO_2-90 wt% HNTs, (k) irradiated Cur-1.5 wt% Ag–TiO_2-90 wt% HNTs and (l) irradiated Cur-3.0 wt% Ag–TiO_2-90 wt% HNTs. The cell viability text was conducted in triplicates and the data were shown by mean ± SD.

From Table 3, the R^2 values obtained from the Korsmeyer-Peppas model were also relatively lower compared to that of the Higuchi model. This implies that the drug release from the HNT and the Ag–TiO_2-HNTs were not diffusion controlled. The higher release exponent values ($n > 0.45$) further confirms that the release cannot be classified as Fickian diffusion.[20]

For all the samples analyzed, the Hixon-Crowell model recorded R^2 values that were lower than the first-order model. This implies that the release does not follow the Hixon-Crowell model. Hixon-Crowell model is used to describe drug release from systems where the diameter of the nanomaterial changes as the release progresses.[57] Due to the insoluble nature of Ag–TiO_2 and HNTs in the release media used in this study, it is

obvious that the release could not follow the Hixon-Crowell model.

3.9 Cytotoxicity studies. The cells which have not been exposed to the nanomaterials were analysed with the trypan blue assay to estimate the live cell concentration. The live cell concentration was estimated to be 5.12×10^6 cells per ml. The cell line (HeLa cell line) was treated with different concentrations of the sample materials and analyzed using the MTT assay. In the treatment processes both irradiated and unirradiated samples were used. The treatment lasted 48 hours whereas the cell viabilities after treatment were determined using the MTT assay. The viability of the drug-treated samples was compared to the untreated HeLa cells known as control. For the free curcumin, as shown in Fig. 8(a), it was observed that curcumin was toxic to the cell line, but its efficacy was not as potent as the curcumin loaded HNT in Fig. 8(b). This confirms that, free curcumin has low bioavailability as reported by many studies[12] whiles HNTs has the potential to be utilized as a vehicle for anti-cancer drug with low bioavailability. Recent publications have concluded that halloysite nanotubes enhances the permeability of drugs into cells improving the drug efficacy.[58,59]

In Fig. 8(c) and (d), an increased in cell viability was observed for the inactivated Ag–TiO_2 samples. The increased was as high as 250% compared to the control value. This implies that, even at the high dose, the unirradiated Ag–TiO_2 NPs samples were not cytotoxic to the HeLa cells. That is the Ag–TiO_2 NPs boosted the cell expression instead of inhibiting it. However, in Fig. 8(e) and (f), activated Ag–TiO_2 NPs samples caused cytotoxicity to the cell line but no total cell death was recorded at the highest concentrations used in this study. The reduction in cell viability confirms the released of reactive oxygen species (ROS) after irradiation by light as reported in various studies. The ROS played an important role in suppressing the cell proliferation.

As shown in Fig. 8(g)–(i), the inactivated drug loaded nanomaterial (Cur-Ag–TiO_2-90 wt% HNT) samples reduced the cell viability at higher particle concentrations. However, when the nanomaterial was irradiated, activated drug loaded nanomaterial (Cur-Ag–TiO_2-90 wt% HNT) samples reduced the cell viability within a concentration range of 20–100 μg mL^{-1} (Fig. 8(j) and (k)). It can be observed that, there were complete cell death at concentration range between 50–100 μg mL^{-1}.

In comparison to that of inactivated drug loaded nanomaterial samples as shown in Fig. 8(g)–(i), it was realized that the cell viability although were decreasing on different concentration of the drug loaded nanomaterial, were not potent as the activated samples. This implies that the cytotoxicity induced on the cell by the activated curcumin loaded Ag–TiO_2-HNTs group was substantially stronger than that induced by free curcumin, activated Ag–TiO_2, and inactivated curcumin loaded Ag–TiO_2-HNTs. These results suggest that the activated curcumin loaded Ag–TiO_2-HNTs nanomaterial which recorded total cell death at higher concentration, exhibited significantly improved antitumor activity. Since curcumin loaded HNTs and activated Ag–TiO_2 recorded a reduction in the cell viability, the much-improved cytotoxicity of the activated curcumin loaded-Ag–TiO_2-HNTs nanomaterial can be attributed to the synergy between the curcumin loaded into the HNTs and the activated Ag–TiO_2 in the cur-Ag–TiO_2-HNTs nanomaterial. The possible explanation for this observation is presented below.

The results obtained from this study demonstrates the importance of combining chemotherapy (curcumin) and photodynamic therapy (Ag–TiO_2) as well as employing halloysite nanotubes as the delivery vehicle for curcumin. Metal oxide nanomaterials such as TiO_2 has the ability to generate reactive oxygen species (ROS) upon solar light irradiation. These generated ROS has been reported to possess the ability to cause cell destruction. The TiO_2 utilized in this study has a wide band gap of ~3.2 eV and as a result, can only be activated in the ultraviolet region of the electromagnetic spectrum. This limitation was addressed by coating the TiO_2 surface with Ag nanoparticles. Coating TiO_2 nanoparticles with Ag nanoparticles shifts the band gap towards that of the visible light region due to the surface plasmonic effect of Ag.[60] Upon irradiation, electrons are excited from the valence band to the conduction band of TiO_2 creating an electron hole pair. However, these electron–hole pair may recombine and hinder the production of ROS. The presence of the Ag also induces localized surface plasmonic resonance (LSPR) effect. LSPR effect creates a strong electric field which enhances charge separation[61] and results in the production of ROS. The photogenerated electrons reacts with H_2O and dissolved oxygen leading to the generation of ROS. The mechanism for the production of ROS is presented in the equations below.

$$TiO_2 + h\nu \rightarrow h^+ + e^-$$

$$e^- + Ag \rightarrow e_{Ag}{}^-$$

$$e_{Ag}{}^- + h\nu \rightarrow e_{LSPR}{}^-$$

$$TiO_2 + e_{LSPR}{}^- \rightarrow h^+ + e^-$$

$$O_2 + e^- \rightarrow {}^{\bullet}O_2{}^-$$

$${}^{\bullet}O_2{}^- + 2H^+ + e^- \rightarrow H_2O_2$$

$$H_2O_2 + e^- \rightarrow {}^{\bullet}OH + OH^-$$

$$H_2O + h^+ \rightarrow {}^{\bullet}OH + H^+$$

$${}^{\bullet}O_2{}^- + \text{cancer cell} \rightarrow \text{cell death}$$

$${}^{\bullet}OH + \text{cancer cell} \rightarrow \text{cell death}$$

Depending on the type of ROS generated, PDT can be classified as type 1 or type II. Type one PDT results from the creation of ${}^{\bullet}O_2{}^-$. This superoxide radical then takes part in a series of reactions resulting in the creation of ${}^{\bullet}OH$. These reactive oxygen species have been reported to be capable of destroying many cancer cells.[6] The irradiated Ag–TiO_2 and curcumin loaded Ag–TiO_2-HNT samples generated ROS that attacked the cancer cells resulting in cell death. ROS creates oxidative damages to cell

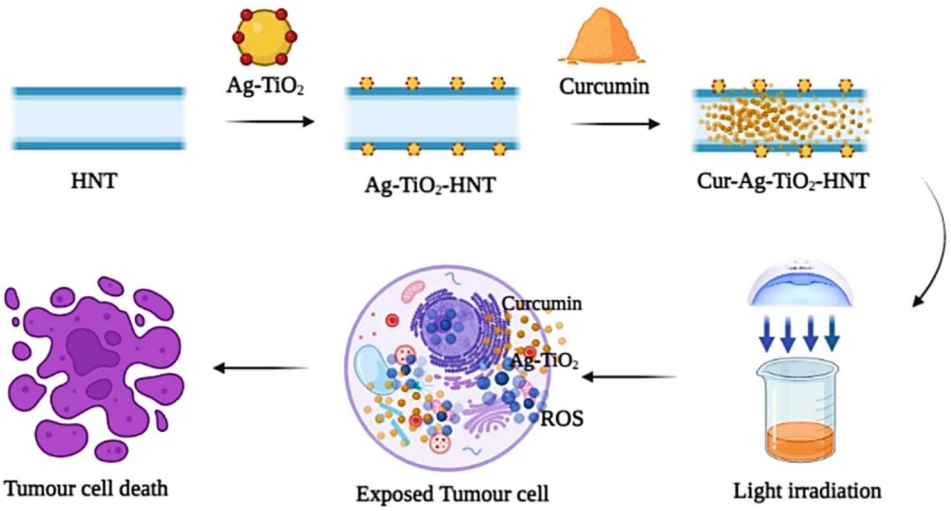

Fig. 9 Schematic illustration showing the mechanism of curcumin loaded Ag–TiO_2-HNTs for synergistic chemotherapy and photodynamic therapy for cancer cells.

membranes, proteins, DNA and mitochondria, and also injure tumor microvasculature hindering blood supply.[62,63]

Commercial curcumin contains three major compounds: curcumin (77%), bisdemethoxycurcumin (3%) and demethoxycurcumin (17%).[8] The anticancer potential of curcumin is as a result of its ability to suppress the proliferation of tumor cells such as breast carcinoma and colon carcinoma, inhibit the activity of kinases, and down-regulate growth factor receptors and transcription factors.[64] The suppression of the proliferation occurs through its effect on the cell cycle and this occurs at different phases of the cell cycle for different cells.[65] In addition, curcumin induces apoptosis in cancer cells either through mitochondria dependent[66] and mitochondria independent[67] processes. Besides these, it is interesting to note that, researchers have reported that curcumin is phototoxic. This means that, curcumin is also a potential photosensitizing drug. These unique anticancer properties of curcumin are responsible for the reduction in the cell viability values reported in this study. Though curcumin has been reported to undergo photodecomposition after exposure to UV or visible light,[68] other study has reported that curcumin has acceptable photostability under UV and visible light irradiation for photodynamic study.[69]

The 0% cell viability values recorded at relatively lower particle concentrations of the irradiated curcumin loaded Ag–TiO_2-HNTs can be attributed to the synergy between the ROS generated from the Ag–TiO_2 nanoparticles, the anticancer properties of curcumin and photosensitizing properties of curcumin (Fig. 9).

4 Conclusion

In this study, curcumin loaded Ag–TiO_2-HNTs combined chemo and photodynamic therapy platform was developed and its efficacy as anti-cancer drug examined. The *in vitro* release process of free curcumin from the curcumin loaded Ag–TiO_2-HNT samples reached their highest release rate between the 24–48 hours. The cumulative release percentage was dependent on the amount of HNTs as well as Ag wt% used in the nanomaterial synthesis. The results from the *in vitro* drug released studies were fitted with kinetic models and revealed that the curcumin loaded HNTs, and curcumin loaded Ag–TiO_2-HNTs nanomaterials followed the first-order and Higuchi model, respectively. Treatment of HeLa cell lines revealed that the viability of the tested cell line decreased with increasing concentrations of the free curcumin, activated Ag–TiO_2 NPs samples and curcumin loaded Ag–TiO_2-HNTs samples. However, it was revealed that, irradiated curcumin loaded Ag–TiO_2-HNTs samples recorded the highest cytotoxicity effect on the HeLa cells lines. This observation was attributed to the synergistic effect of ROS generated from the Ag–TiO_2 and the anticancer and photosensitizing effect of curcumin released from the HNTs on the HeLa cells. This result revealed the potential application of activated curcumin loaded Ag–TiO_2-HNTs nanomaterial as a potential anticancer drug.

Data availability

The raw/processed data required to reproduce these findings cannot be shared at this time as the data also forms part of an ongoing study.

Conflicts of interest

There are no conflicts to declare.

References

1 World Health Organisation, *World cancer report: cancer research for cancer prevention*, International Agency for Research on Cancer, Lyon, 2020th edn, 2020.

2 X. Liang, C. Chen, Y. Zhao, P. C. Wang, Circumventing tumor resistance to chemotherapy by nanotechnology, *Multi-Drug Resistance in Cancer*, 2010, vol. 596, pp. 467–488.
3 T. B. Ling and M. E. Norhaizan, Curcumin Combination Chemotherapy : The Implication and Efficacy in Cancer, *Molecules*, 2019, **24**(1), 1–21.
4 K. Sak, Chemotherapy and Dietary Phytochemical Agents, *Chemother. Res. Pract.*, 2012, **2012**, 1–11, DOI: **10.1155/2012/282570**.
5 R. W. Johnstone, A. A. Ruefli and S. W. Lowe, Apoptosis : A Link between Cancer Genetics and Chemotherapy, *Cell*, 2002, **108**(2), 153–164.
6 P. Kovacic, Unifying mechanism for anticancer agents involving electron transfer and oxidative stress: Clinical implications, *Med. Hypotheses*, 2007, **69**(3), 510–516, DOI: **10.1016/j.mehy.2006.08.046**.
7 A. Goel, A. B. Kunnumakkara and B. B. Aggarwal, Curcumin as 'Curecumin': from kitchen to clinic, *Biochem. Pharmacol.*, 2008, **75**(4), 87–809, DOI: **10.1016/j.bcp.2007.08.016**.
8 B. Aggarwal, A. KUMAR and A. C. Bharti, Anticancer Potential of Curcumin : Preclinical and Clinical Studies, *Anticancer Res.*, 2003, **23**, 363–398.
9 M. Huang, J. J. Lu and J. Ding, Natural Products in Cancer Therapy: Past, Present and Future, *Nat. Prod. Bioprospect.*, 2021, **11**(1), 5–13, DOI: **10.1007/s13659-020-00293-7**.
10 B. B. Aggarwal, C. Sundaram, N. Malani and H. Ichikawa, Curcumin: the Indian solid gold, *Adv. Exp. Med. Biol.*, 2006, 1–76.
11 N. A. N. Hanafy, S. Leporatti and M. El-kemary, Mucoadhesive curcumin crosslinked carboxy methyl cellulose might increase inhibitory efficiency for liver cancer treatment, *Mater. Sci. Eng., C*, 2020, **116**, 1–11, DOI: **10.1016/j.msec.2020.111119**.
12 P. Anand, A. B. Kunnumakkara, R. A. Newman and B. B. Aggarwal, Bioavailability of Curcumin: Problems and Promises, *Mol. Pharm.*, 2007, **4**(6), 807–818, DOI: **10.2174/09298673113209990120**.
13 M. Liu, *et al.*, Functionalized halloysite nanotube by chitosan grafting for drug delivery of curcumin to achieve enhanced anticancer efficacy, *J. Mater. Chem. B*, 2016, **4**(13), 2253–2263, DOI: **10.1039/c5tb02725j**.
14 A. Stavitskaya, *et al.*, Architectural design of core–shell nanotube systems based on aluminosilicate clay, *Nanoscale Adv.*, 2022, **4**(13), 2823–2835, DOI: **10.1039/d2na00163b**.
15 M. Massaro, *et al.*, Applied clay science chemical and biological evaluation of cross-linked halloysite-curcumin derivatives, *Appl. Clay Sci.*, 2020, **184**, 105400, DOI: **10.1016/j.clay.2019.105400**.
16 C. Dionisi, *et al.*, Halloysite clay nanotubes as carriers for curcumin: characterization and application, *IEEE Trans. Nanotechnol.*, 2017, **15**(5), 720–724, DOI: **10.1109/TNANO.2016.2524072**.
17 M. Massaro, G. Lazzara, S. Milioto, R. Noto and S. Riela, Covalently modified halloysite clay nanotubes: synthesis, properties, biological and medical applications, *J. Mater. Chem. B*, 2017, **5**(16), 2867–2882, DOI: **10.1039/c7tb00316a**.
18 Y. Lvov, A. Aerov and R. Fakhrullin, Clay nanotube encapsulation for functional biocomposites, *Adv. Colloid Interface Sci.*, 2014, **207**(1), 189–198, DOI: **10.1016/j.cis.2013.10.006**.
19 A. Khdair, *et al.*, Nanoparticle-mediated combination chemotherapy and photodynamic therapy overcomes tumor drug resistance, *J. Controlled Release*, 2010, **141**(2), 137–144, DOI: **10.1016/j.jconrel.2009.09.004**.
20 E. Nyankson, *et al.*, Chitosan-coated halloysite nanotubes as vehicle for controlled drug delivery to MCF-7 cancer cells *in vitro*, *Materials*, 2021, **14**(11), 1–16, DOI: **10.3390/ma14112837**.
21 X. Dai, T. Du and K. Han, Engineering Nanoparticles for Optimized Photodynamic Therapy, *ACS Biomater. Sci. Eng.*, 2019, **5**(12), 6342–6354, DOI: **10.1021/acsbiomaterials.9b01251**.
22 X. Li, S. Lee and J. Yoon, Supramolecular photosensitizers rejuvenate photodynamic therapy, *Chem. Soc. Rev.*, 2018, **47**(4), 1174–1188, DOI: **10.1039/c7cs00594f**.
23 Photodynamic Therapy, *Mayo Clinic*, **https://www.mayoclinic.org/tests-procedures/photodynamic-therapy/about/pac-20385027**, accessed Feb. 17, 2021.
24 L. B. Josefsen and R. W. Boyle, Photodynamic therapy and the development of metal-based photosensitisers, *Met.-Based Drugs*, 2007, **2008**, 1–24, DOI: **10.1155/2008/276109**.
25 D. Ziental, *et al.*, Titanium dioxide nanoparticles: prospects and applications in medicine, *Nanomaterials*, 2020, **10**(387), 1–31, DOI: **10.3390/nano10020387**.
26 N. Lagopati, *et al.*, Effect of nanostructured TiO_2 crystal phase on photoinduced apoptosis of breast cancer epithelial cells, *Int. J. Nanomed.*, 2014, **9**(1), 3219–3230, DOI: **10.2147/IJN.S62972**.
27 M. Ahamed, M. A. M. Khan, M. J. Akhtar, H. A. Alhadlaq and A. Alshamsan, Ag-doping regulates the cytotoxicity of TiO_2 nanoparticles *via* oxidative stress in human cancer cells, *Sci. Rep.*, 2017, **7**(1), 1–14, DOI: **10.1038/s41598-017-17559-9**.
28 A. Fujishima and K. Honda, Electrochemical Photolysis of Water at a Semiconductor Electrode One and Two-dimensional Structure of Alpha-Helix and Beta-Sheet Forms of Poly(L-Alanine) shown by Specific Heat Measurements at Low Temperatures (1.5–20 K), *Nature*, 1972, **238**(5358), 37–38.
29 P. Magalhães, L. Andrade, O. C. Nunes and A. Mendes, Titanium dioxide photocatalysis: Fundamentals and application on photoinactivation, *Rev. Adv. Mater. Sci.*, 2017, **51**(2), 91–129.
30 H.-M. H. Xiaojia He, W. G. Aker, M.-Ju Huang and J. D. Watts, Metal Oxide Nanomaterials in Nanomedicine: Applications in Photodynamic Therapy and Potential Toxicity, *Curr. Top. Med. Chem.*, 2015, **15**(18), 1887–1900.
31 L. M. Santos, *et al.*, Structural characterization of Ag-doped TiO_2 with enhanced photocatalytic activity, *RSC Adv.*, 2015, **5**, 103752–103759, DOI: **10.1039/C5RA22647C**.
32 Z. Jiang, *et al.*, Silver-deposited, Nitrogen-doped Yolk-shell Mesoporous TiO_2 Hollow Microspheres with Enhanced Visible Light Photocatalytic Activity, *Nanoscale*, 2014, **7**(2), 1–43, DOI: **10.1039/C4NR05963H**.

33 T. Liu, B. Li, Y. Hao, F. Han, L. Zhang and L. Hu, A general method to diverse silver/mesoporous–metal-oxide nanocomposites with plasmon-enhanced photocatalytic activity, *Appl. Catal., B*, 2015, **165**, 378–388, DOI: 10.1016/j.apcatb.2014.10.041.

34 Z. Youssef, TiO_2 Nanoparticles Coupled To Photosensitizers For Applications In Photocatalysis And Photodynamic Therapy, *Chem. Process Eng.*, 2017, 1–306.

35 R. Fujiwara, Y. Luo, T. Sasaki, K. Fujii, H. Ohmori and H. Kuniyasu, Cancer therapeutic effects of titanium dioxide nanoparticles are associated with oxidative stress and cytokine induction, *Pathobiology*, 2015, **82**(6), 243–251, DOI: 10.1159/000439404.

36 H. Zhang and G. Chen, Potent antibacterial activities of Ag/TiO_2 nanocomposite powders synthesized by a one-pot sol–gel method, *Environ. Sci. Technol.*, 2009, **43**(8), 2905–2910, DOI: 10.1021/es803450f.

37 C. M. Girish, *et al.*, Rapid detection of oral cancer using Ag–TiO_2 nanostructured surface-enhanced Raman spectroscopic substrates, *J. Mater. Chem. B*, 2014, **2**(8), 989–998, DOI: 10.1039/c3tb21398f.

38 R. R. Price, B. P. Gaber and Y. Lvov, *In vitro* release characteristics of tetracycline HC1, khellin and nicotinamide adenine dinucleotide from halloysite; a cylindrical mineral, *J. Microencapsulation*, 2001, **18**(6), 713–722, DOI: 10.1080/02652040010019532.

39 E. Nyankson, *et al.*, Microwave- And Formaldehyde-Assisted Synthesis of Ag–Ag_3PO_4 with Enhanced Photocatalytic Activity for the Degradation of Rhodamine B Dye and Crude Oil Fractions, *ACS Omega*, 2020, **5**(23), 13641–13655, DOI: 10.1021/acsomega.0c00670.

40 M. N. Siddique, A. Ahmed and P. Tripathi, Electric transport and enhanced dielectric permittivity in pure and Al doped NiO nanostructures, *J. Alloys Compd.*, 2018, **735**, 516–529, DOI: 10.1016/j.jallcom.2017.11.114.

41 T. Ali, A. Ahmed, U. Alam, I. Uddin, P. Tripathi and M. Muneer, Enhanced photocatalytic and antibacterial activities of Ag-doped TiO_2 nanoparticles under visible light, *Mater. Chem. Phys.*, 2018, **212**, 325–335, DOI: 10.1016/j.matchemphys.2018.03.052.

42 X. Li, *et al.*, Determination of band gaps of self-assembled carbon nanotube films using Tauc/Davis-Mott model, *Appl. Phys. A: Mater. Sci. Process.*, 2009, **97**(2), 341–344, DOI: 10.1007/s00339-009-5330-z.

43 D. Papoulis, *et al.*, Halloysite-TiO_2 nanocomposites: synthesis, characterization and photocatalytic activity, *Appl. Catal., B*, 2013, **132–133**, 416–422, DOI: 10.1016/j.apcatb.2012.12.012.

44 X. Chen, L. Q. Zou, J. Niu, W. Liu, S. F. Peng and C. M. Liu, The stability, sustained release and cellular antioxidant activity of curcumin nanoliposomes, *Molecules*, 2015, **20**(8), 14293–14311, DOI: 10.3390/molecules200814293.

45 G. Kandregula, K. V. Rao and S. Chidurala, Synthesis of TiO_2 Nanoparticles from Orange Fruit Waste, *Int. J. Multidiscip. Adv. Res. Trends*, 2015, **II**, 82–90.

46 A. N. Murashkevich, A. S. Lavitskaya, T. I. Barannikova and I. M. Zharskii, Infrared absorption spectra and structure of TiO_2–SiO_2 composites, *J. Appl. Spectrosc.*, 2008, **75**(5), 730–734, DOI: 10.1007/s10812-008-9097-3.

47 Y. Du, Y. Fu, X. Gao, W. He and P. Zheng, Halloysite-TiO_2–Ag composites: preparation, characterization and photodegradation, *IOP Conf. Ser.: Mater. Sci. Eng.*, 2020, **729**(1), 1–7, DOI: 10.1088/1757-899X/729/1/012087.

48 E. Nyankson, *et al.*, Synthesis and Application of Fe-Doped TiO_2-Halloysite Nanotubes Composite and Their Potential Application in Water Treatment, *Hindawi*, 2019, **2019**, 1–15.

49 Y. Zhang, L. Fu and H. Yang, Insights into the physicochemical aspects from natural halloysite to silica nanotubes, *Colloids Surf., A*, 2012, **414**, 115–119, DOI: 10.1016/j.colsurfa.2012.08.003.

50 E. G. Bediako, *et al.*, Modified halloysite nanoclay as a vehicle for sustained drug delivery, *Heliyon*, 2018, **4**(7), 1–21, DOI: 10.1016/j.heliyon.2018.e00689.

51 D. Papoulis, *et al.*, Palygorskite- and Halloysite-TiO_2 nanocomposites: synthesis and photocatalytic activity, *Appl. Clay Sci.*, 2010, **50**(1), 118–124, DOI: 10.1016/j.clay.2010.07.013.

52 E. Nyankson, O. Olasehinde, V. T. John and R. B. Gupta, Surfactant-Loaded Halloysite Clay Nanotube Dispersants for Crude Oil Spill Remediation, *Ind. Eng. Chem. Res.*, 2015, **54**(38), 9328–9341, DOI: 10.1021/acs.iecr.5b02032.

53 O. Owoseni, *et al.*, Release of surfactant cargo from interfacially-active halloysite clay nanotubes for oil spill remediation, *Langmuir*, 2014, **30**(45), 13533–13541, DOI: 10.1021/la503687b.

54 R. El Kurdi and D. Patra, Tuning the surface of Au nanoparticles using poly(ethylene glycol)-block-poly(propylene glycol)-block-poly(ethylene glycol): Enzyme free and label free sugar sensing in serum samples using resonance Rayleigh scattering spectroscopy, *Phys. Chem. Chem. Phys.*, 2018, **20**(14), 9616–9629, DOI: 10.1039/c8cp01147h.

55 J. Weng, H. H. Y. Tong and S. F. Chow, *In Vitro* Release Study of the Polymeric Drug Nanoparticles: Development and Validation of a Novel Method, *MDPI*, 2020, **732**(12), 1–18.

56 A. R. Chandrasekaran, C. Y. Jia, C. S. Theng, T. Muniandy, S. Muralidharan and S. Arumugam, *In vitro* studies and evaluation of metformin marketed tablets-Malaysia, *J. Appl. Pharm. Sci.*, 2011, **01**(05), 214–217.

57 S. Dash, P. N. Murthy, L. Nath and P. Chowdhury, Kinetic modeling on drug release from controlled drug delivery systems, *Acta Pol. Pharm. Drug Res.*, 2010, **67**(3), 217–223.

58 E. Carazo, *et al.*, Halloysite nanotubes as tools to improve the actual challenge of fixed doses combinations in tuberculosis treatment, *J. Biomed. Mater. Res., Part A*, 2019, **107**(7), 1513–1521, DOI: 10.1002/jbm.a.36664.

59 V. Vergaro, Y. M. Lvov and S. Leporatti, Halloysite clay nanotubes for resveratrol delivery to cancer cells, *Macromol. Biosci.*, 2012, **12**(9), 1265–1271, DOI: 10.1002/mabi.201200121.

60 P. Navabpour, S. Ostovarpour, J. Hampshire, P. Kelly, J. Verran and K. Cooke, The effect of process parameters on the structure, photocatalytic and self-cleaning properties of TiO_2 and Ag–TiO_2 coatings deposited using

reactive magnetron sputtering, *Thin Solid Films*, 2014, **571**(P1), 75–83, DOI: **10.1016/j.tsf.2014.10.040**.

61 J. Fang, *et al.*, Mesoporous plasmonic Au–TiO_2 nanocomposites for efficient visible-light-driven photocatalytic water reduction, *Int. J. Hydrogen Energy*, 2012, **37**(23), 17853–17861, DOI: **10.1016/j.ijhydene.2012.09.023**.

62 V. H. Fingar, *et al.*, Analysis of acute vascular damage after photodynamic therapy using benzoporphyrin derivative (BPD), *Br. J. Cancer*, 1999, **79**(11–12), 1702–1708, DOI: **10.1038/sj.bjc.6690271**.

63 C. Yi, *et al.*, Nanoscale ZnO-based photosensitizers for photodynamic therapy, *Photodiagn. Photodyn. Ther.*, 2020, **30**, 101694, DOI: **10.1016/j.pdpdt.2020.101694**.

64 J. K. L. Y. C. Chen, T. C. Kuo and S. Y. Lin-Shiau, Induction of HSP70 gene expression by modulation of Ca(+2) ion and cellular p53 protein by curcumin in colorectal carcinoma cells, *Mol. Carcinog. Publ. Coop. with Univ. Texas MD Anderson Cancer Center*, 1996, **17**(4), 224–234.

65 H. W. Chen and H. C. Huang, Effect of curcumin on cell cycle progression and apoptosis in vascular smooth muscle cells, *Br. J. Pharmacol.*, 1998, **124**(6), 1029–1040, DOI: **10.1038/sj.bjp.0701914**.

66 S. Bhaumik, R. Anjum, N. Rangaraj, B. V. V. Pardhasaradhi and A. Khar, Curcumin mediated apoptosis in AK-5 tumor cells involves the production of reactive oxygen intermediates, *FEBS Lett.*, 1999, **456**(2), 311–314, DOI: **10.1016/S0014-5793(99)00969-2**.

67 K. Piwocka, *et al.*, A novel apoptosis-like pathway, independent of mitochondria and caspases, induced by curcumin in human lymphoblastoid T (Jurkat) cells, *Exp. Cell Res.*, 1999, **249**(2), 299–307, DOI: **10.1006/excr.1999.4480**.

68 H. H. Tønnesen, J. Karlsen and G. B. van Henegouwen, Studies on curcumin and curcuminoids VIII. Photochemical stability of curcumin, *Z. Lebensm. Unters. Forsch.*, 1986, **183**(2), 116–122, DOI: **10.1007/BF01041928**.

69 T. Haukvik, E. Bruzell, S. Kristensen and H. H. Tønnesen, Photokilling of bacteria by curcumin in different aqueous preparations. Studies on curcumin and curcuminoids XXXVII, *Die Pharm. Int. J. Pharm. Sci.*, 2009, **64**(10), 666–673, DOI: **10.1691/ph.2009.0000**.